Journal of Biomechanics 94 (2019) 219–223

Contents lists available at ScienceDirect

Journal of Biomechanics

journal homepage: www.elsevier.com/locate/jbiomech
www.JBiomech.com

Short communication

Quantification of regional right ventricular strain in healthy rats using 3D spiral cine dense MRI

Zhan-Qiu Liu [a], Xiaoyan Zhang [a,b], Jonathan F. Wenk [a,c,*]

[a] Department of Mechanical Engineering, University of Kentucky, Lexington, KY, United States
[b] Department of Bioengineering, University of California, San Diego, CA, United States
[c] Department of Surgery, University of Kentucky, Lexington, KY, United States

ARTICLE INFO

Article history:
Accepted 22 July 2019

Keywords:
3D DENSE plugin for Crescent Organ
3D lagrangian strain
Surface fitting

ABSTRACT

Statistical data from clinical studies suggests that right ventricular (RV) circumferential strain (E_{cc}) and longitudinal strain (E_{ll}) are significant biomarkers for many cardiovascular diseases. However, a detailed and regional characterization of these strains in the RV is very limited. In the current study, RV images were obtained with 3D spiral cine DENSE MRI in healthy rats. An algorithm for surface growing was proposed in order to fit irregular topology. Specifically, a new custom plugin for the DENSEanalysis program, called 3D DENSE Plugin for Crescent Organ, was developed for surface reconstruction and precise segmentation of organs with sharp curvature, such as the murine RV. The RV free wall (RVFW) was divided into three longitudinal thirds (i.e., basal, middle, and apical) with each one partitioned into circumferential fourths (i.e., anterior, anteriorlateral, inferiorlateral and inferior). Peak systolic strains were quantified for each segment and comparisons were performed statistically. The inclusion of a new plugin was able to generate global values for E_{cc} and E_{ll} that are in good agreement with previous findings using MRI. Despite no regional variation found in the peak E_{cc}, the peak E_{ll} exhibited regional variation at the anterior side of the RV, which is potentially due to differences in biventricular torsion at the RV insertion point and fiber architecture. These results provide fundamental insights into the regional contractile function of the RV in healthy rat and could act as a normative baseline for future studies on regional changes induced by disease or treatment.

1. Introduction

According to the American Heart Association, the number of American adults suffering from heart failure (HF) rose from 5.7 million between 2009 and 2012 to 6.2 million between 2013 and 2016 (Benjamin Emelia et al., 2019). More importantly, an increasing number of studies have observed that abnormalities in organ-level cardiac function of the right ventricle (RV) can serve as predictors of disease presence. For example, an impaired RV ejection fraction significantly increased 2-year mortality in patients with HF and coronary artery disease (Polak et al., 1983). Additionally, impaired RV end-diastolic volume was found to be significantly correlated with the presence of arrhythmogenic RV cardiomyopathy (ARVC) (Vigneault et al., 2016).

Furthermore, clinical studies (Derrick et al., 2001; Eyskens et al., 2004) have shown that reduced RV deformation is a crucial biomarker of global cardiac dysfunction. In particular, a significant decrease was found in both RV peak longitudinal and circumferential strains in patients with ARVC, using cine Steady State Free Precession (SSFP) MRI (Vigneault et al., 2016). Additionally, RV free wall (RVFW) peak longitudinal strain, predicted by speckle-tracking echocardiography, was used to assess the 18-month survival rate of patients with pulmonary hypertension (PH) (Fine et al., 2013a) and predict HF with preserved ejection fraction (Morris et al., 2017). In patients with pulmonary arterial hypertension (PAH), RV HF and 2-year mortality were forecast with echocardiography through RV peak longitudinal strain (Sachdev et al., 2011). Since patients with PAH have a high mortality rate (Ryan et al., 2015), abnormalities in RV deformation should be a critical focal point during disease management.

The rat has proven to be a useful model in cardiac research of the RV. For example, previous studies have used rats to investigate remedies for PH and RV HF (Labinskyy et al., 2008; Mouchaers et al., 2010; Sawamura et al., 2009). Since impaired RV strains are strongly correlated with the presence of cardiovascular diseases, establishing reproducible baselines of these strains is essential.

* Corresponding author at: University of Kentucky, Department of Mechanical Engineering 269 Ralph G. Anderson Building, Lexington, KY 40506-0503, United States.
E-mail address: jonathan.wenk@uky.edu (J.F. Wenk).

https://doi.org/10.1016/j.jbiomech.2019.07.026
0021-9290/

Recently, invasive techniques utilizing sonomicrometry crystal tracking (Meador et al., 2018) were used to assess RV strains. However, imaging methods are more widely used in studies due to their non-invasive nature. In particular, Spatial Modulation of Magnetization tagged MRI was used to evaluate RV deformation (Haber et al., 2000), but the thin RV wall made tracking the entire lengths of the tags difficult. Additionally, cine SSFP MRI was also used to quantify RV strains (Lollert et al., 2018; Nucifora et al., 2016). However, these strains are much less reproducible than those from Displacement ENcoding with Stimulated Echoes (DENSE) MRI (Haggerty et al., 2013).

To date, there are limited studies conducted on the RV with DENSE MRI, including no published study using a rat model and DENSE MRI. Therefore, the aim of the current study was to investigate the normal state of cardiac mechanics in the rat RV using DENSE MRI. In the process, an algorithm of mesh growing was proposed for irregular topology and a new plugin was developed for the DENSEanalysis program, which allowed for better assessment of the sharp curvature seen in the rat RV. The results establish a baseline for deformation in a healthy heart, which can later be used to compare to pathological states.

2. Methods

2.1. Animal preparation and image acquisition

Details related to the animal preparation and cardiac MRI acquisition are provided in depth in previous studies (Zhang et al., 2019, 2017). It should be noted that all animal procedures were approved by the Institutional Animal Care and Use Committee at the University of Kentucky and were in agreement with the National Institute of Health's guidelines for the care and use of laboratory animals (NIH Publication 85-23, revised 1996). Briefly, the 3D spiral cine DENSE images were acquired in healthy female Sprague-Dawley rats, which were ~6 months of age. Cardiac MRI was performed on a 7-Tesla Bruker ClinScan system (Bruker, Ettlingen, Germany) equipped with a 2 × 2 hydrogen phased-array coil and a gradient system (strength: 450 mT/m; slew rate: 4500 T/m/s). Acquisition was conducted using both cardiac and respiratory gating with a repetition time of 7.4 ms and an echo time of 1 ms. Other relevant acquisition parameters include: pixel size = 0.357 × 0.357 mm, field of view = 50 × 50 mm, slice thickness = 1.3 mm, spiral interleaves = 36, and displacement encoding frequency = 0.3 cycles/mm. Images from seven of these previously scanned animals were selected to be analyzed in the current study. Image selection was based on clarity of the RV wall throughout the entire cardiac cycle. More specifically, only images where all regions of the RV wall were fully resolved were used in this study.

2.2. Image and strain analysis

Biventricular endocardial and epicardial borders were manually traced over the whole cardiac cycle (Fig. 1A) using an open-source application DENSEanalysis (Gilliam et al., 2016; Spottiswoode et al., 2007). Subsequently, the DENSE3D Plugin (Suever, 2016) was used to fit the epicardial, LV endocardial, and RV endocardial surface meshes with the short-axis (SA) biventricular contours at ED. Although the plugin was validated in the human RV (Suever et al., 2017), it was determined that this plugin was unable to fit a surface to the sharp curvature seen in the rat RV (blue curves in Fig. 2A). This is mainly caused by the geometry at the RV insertion point locations (Fig. 2E), which is more complex than the human RV.

In order to reconstruct and segment the RV endocardial surface mesh, a new custom plugin, 3D DENSE Plugin for Crescent Organ, was developed and is available for use with the DENSEanalysis program via GitHub (Liu, 2018). In terms of the reconstruction, the RV surface mesh was propagated in the form of a surface growing towards manually selected guiding points using a custom iteration algorithm. Specifically, starting with an initial surface mesh (Fig. 2A) exported from the DENSE3D Plugin, each mesh vertex $\hat{\boldsymbol{x}}$ was iteratively propagated over a displacement vector $\hat{\boldsymbol{D}}(\hat{\boldsymbol{x}})$:

$$\hat{\boldsymbol{D}}(\hat{\boldsymbol{x}}) = \left[\sum_{i=1}^{M} \omega_i' \hat{\boldsymbol{\phi}}(\|\hat{\boldsymbol{x}} - \hat{\boldsymbol{x}}_i\|) \cdot \hat{\boldsymbol{n}}\right] \hat{\boldsymbol{n}} \tag{1}$$

where $\hat{\boldsymbol{n}}$ is the unit surface normal vector corresponding to $\hat{\boldsymbol{x}}$; M is the number of neighboring fitted points $\hat{\boldsymbol{x}}_i$ on the delineated contours within a radius of r to $\hat{\boldsymbol{x}}$; $\hat{\boldsymbol{\phi}}$ is the vector function proportional to $\|\hat{\boldsymbol{x}} - \hat{\boldsymbol{x}}_i\|$; and the adjusted weight ω_i' is defined by

$$\omega_i' = \begin{cases} W\left(\frac{1}{\|\hat{\boldsymbol{x}} - \hat{\boldsymbol{x}}_i\|}\right), & \text{if } \hat{\boldsymbol{x}}_i \text{ is outside the boundary set } \mathcal{L} \\ W\left(\frac{1}{\|\hat{\boldsymbol{x}} - \hat{\boldsymbol{x}}_i\|}\right) + \Psi\left(\frac{1}{\|\hat{\boldsymbol{x}} - \hat{\boldsymbol{x}}_i\|}\right), & \text{if } \hat{\boldsymbol{x}}_i \text{ is inside the boundary set } \mathcal{L} \end{cases} \tag{2}$$

where $\mathcal{L}$ is a boundary set of custom-sized spherical regions (yellow masks in Fig. 2B–D) centered at corresponding manually selected guiding points (asterisks in Fig. 2B–D); W and Ψ are the scalar functions inversely proportional to $\|\hat{\boldsymbol{x}} - \hat{\boldsymbol{x}}_i\|$. The radius r was linearly increased from an automatically-defined lower bound to a custom upper bound over each subsequent iteration. After a converged number of iterations, different guiding points were selected. This was followed by re-running the above iteration algorithm until a satisfactory topology was achieved, where the mesh elements were all uniform in size and regularity (Fig. 2D). Regarding the circumferential segmentation, parameterization was performed for longitudinally varying anterior and inferior RV insertion points, respectively. To put another way, the parameterization was able to detect that the RV insertion points shift their circumferential location when moving between short axis slices. The parameterization methodology introduced by Suever et al. (2017) was used in all segmentations. The wedge-shaped RVFW was segmented from the LVFW and the interventricular septum (Fig. 2E). Following the longitudinal segmentation, the septal insertion was excluded from the region of interest during strain analysis (Fig. 2F), since it is not possible to fully reconstruct the sharp corners of the RV.

The strain analysis was conducted using the approach outlined in Suever et al. (2017). Briefly, following semi-automatic phase unwrapping (Spottiswoode et al., 2007), the 3D Lagrangian displacement field, as a function of time, was acquired by voxel interpolation and then a local coordinate system was created within each element of the endocardial mesh (Suever et al., 2017). Finally, the Lagrangian strain tensor at each element was calculated using the displacements and then transformed into the local coordinate system, resulting in a tensor that consisted of 6 components (E_{rr}, E_{cc}, E_{ll}, E_{cl}, E_{rl}, and E_{rc}). For regional strain analysis, the RVFW was divided into circumferential fourths (i.e., anterior, anteriorlateral, inferiorlateral and inferior segments) and longitudinal thirds (i.e., basal, middle, and apical segments), which produced 12 segments (Fig. 3). This is consistent with a previous study by Suever et al. (2017), with the only difference being an additional apical region, which is not used here.

2.3. Statistics

All data are presented as mean ± standard deviation. Multiple comparisons between 4 groups (i.e., anterior, anteriorlateral, inferiorlateral and inferior segments) were performed using one-way ANOVA with post-hoc Bonferroni t-tests. Comparisons between 2 groups were conducted with unpaired Student's *t*-tests assuming equal variances. A value of $p < 0.05$ was considered significant.

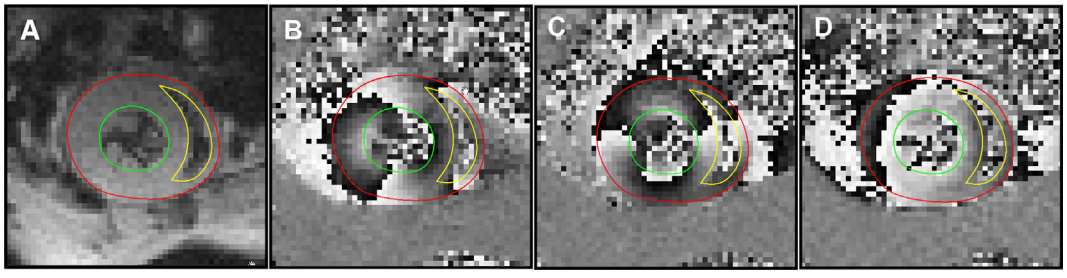

Fig. 1. Representative end-systolic 3D spiral cine DENSE images from one mid-ventricular short-axis slice of a rat left and right ventricle viewed from the apex. (A) A magnitude-reconstructed image; (B) a phase image encoded for x-displacement; (C) a phase image encoded for y-displacement; (D) a phase image encoded for z-displacement.

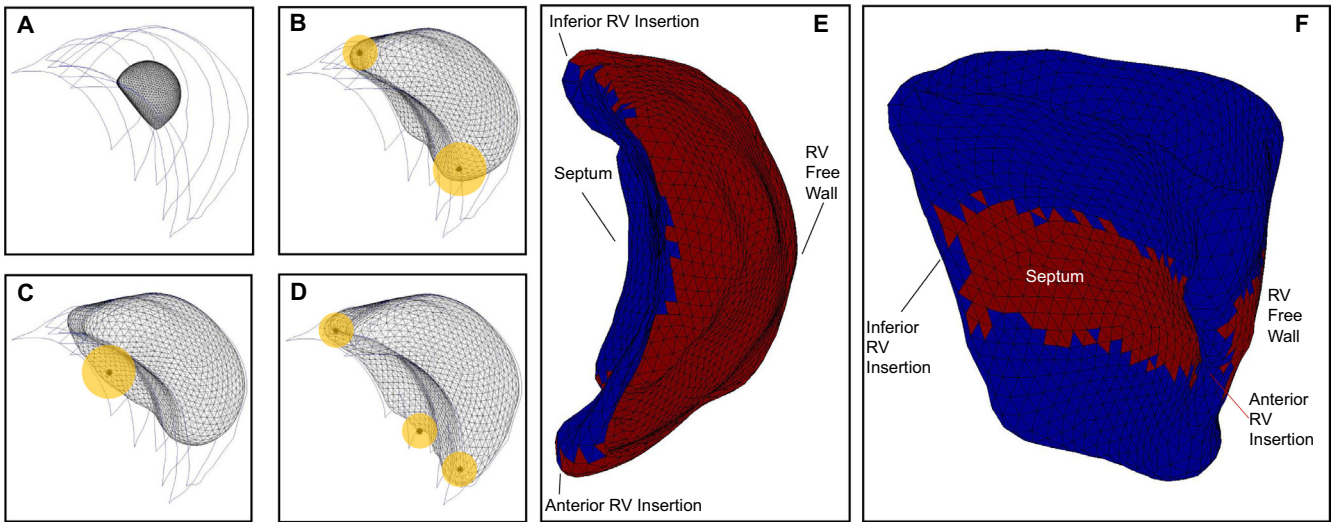

Fig. 2. 3D DENSE Plugin for crescent organ. (A) An initial RV endocardial surface mesh; (B-D) Reconstruction of the RV mesh by surface growing; blue curves are a stack of manually delineated ED SA contours; draggable guiding points are indicated by asterisks; pseudo sphere surfaces with custom radius are depicted by yellow masks; (E) circumferential segmentation for the RV free wall depicted by the red region and viewed from the base; (F) mid-ventricular RV free wall excluding septal insertion. (For interpretation of the references to colour in this figure legend, the reader is referred to the web version of this article.)

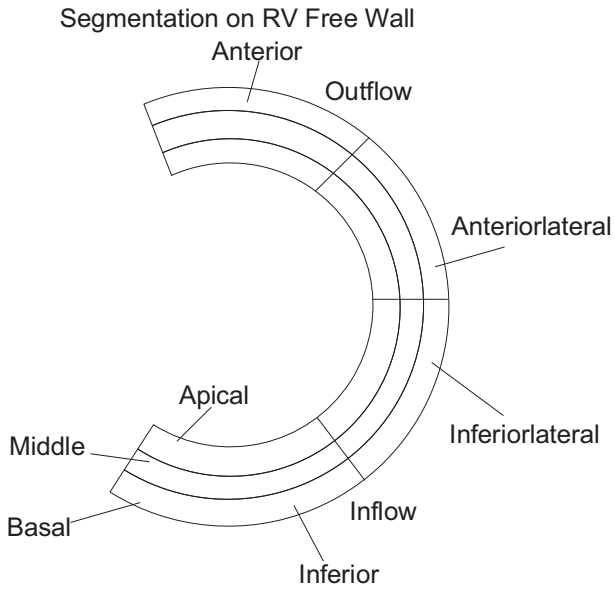

Fig. 3. Diagram of ventricular myocardial segmentation on RV free wall.

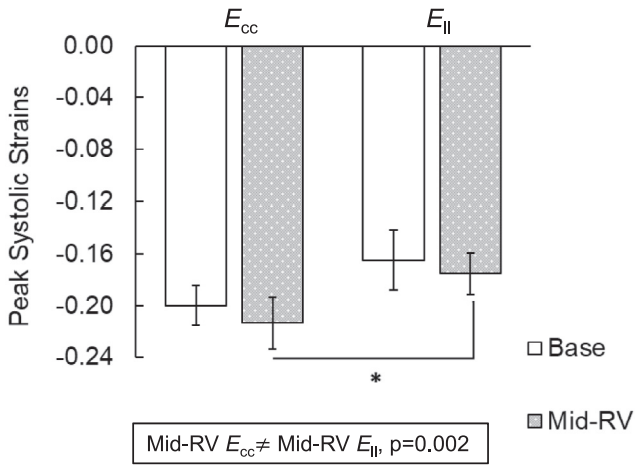

Fig. 4. Distribution of peak systolic strains at base and mid-ventricle of right ventricle. Peak systolic strains for normal components (E_{cc} and E_{ll}) were averaged over the entire slice at either basal [Base] or mid-ventricular [Mid-RV] of rat RVs. *$p < 0.05$.

3. Result

3.1. Distribution of peak systolic strains at the base and mid-ventricle of the RV

Peak strains at the base and mid-ventricle of the RV are shown in Fig. 4. There was no significant difference in either the peak circumferential strain (E_{cc}) or peak longitudinal strain (E_{ll}) when comparing within the basal and mid-ventricular segments of the RV free wall. At the base, no differences were noted when comparing peak E_{cc} to peak E_{ll}. However, peak E_{cc} was significantly higher than peak E_{ll} at mid-ventricle.

3.2. Distribution of peak systolic strains in the RV base

As presented in Fig. 5A, no differences were found in E_{cc} among the anterior, anterolateral, inferolateral, and inferior segments of the RV basal free wall. Nevertheless, E_{ll} in the RV basal free wall was significantly lower in the anterior segment compared to the anterolateral, inferolateral, and inferior segments, respectively (Fig. 5B).

3.3. Distribution of peak systolic strains in the RV Mid-ventricle

The strain component E_{cc} exhibited similar peak systolic values in the anterior, anterolateral, inferolateral, and inferior segments of the RV mid-ventricular free wall (Fig. 6A). However, E_{ll} in the RV middle free wall was significantly lower in the anterior segment compared to the anterolateral, inferolateral, and inferior segments, respectively (Fig. 6B). This mirrors the trend seen in the basal region of the RV free wall. It should be noted that the strains were not analyzed in the apical region, which is discussed in the limitations.

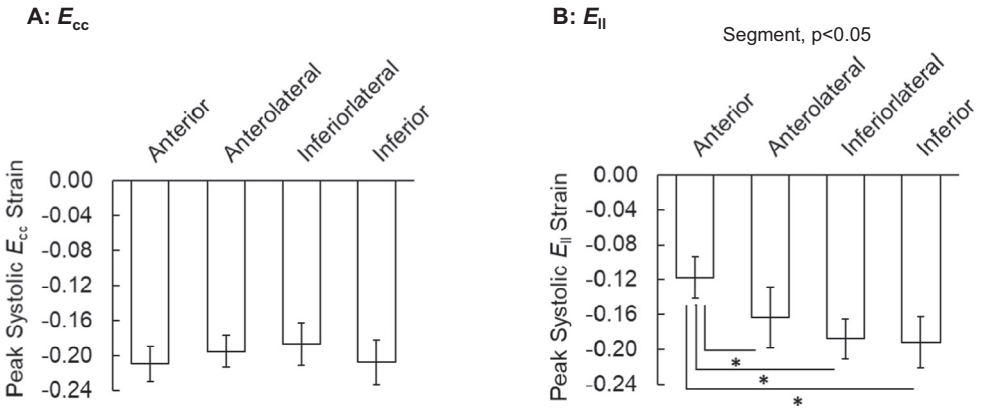

Fig. 5. Distribution of peak systolic strains in the RV base. Peak systolic E_{cc} (A) and E_{ll} (B) were computed for the four circumferential regions of the rat basal RVs. *p < 0.05.

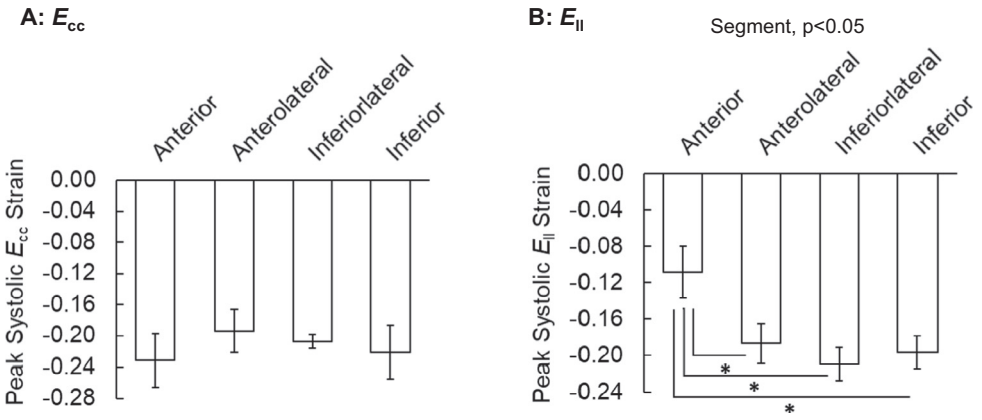

Fig. 6. Distribution of peak systolic strains in the RV mid-ventricle. Peak systolic E_{cc} (A) and E_{ll} (B) were computed for the four circumferential regions of the rat mid-RVs. *p < 0.05.

4. Discussion

In the current study, the circumferential and longitudinal strains were investigated over the base and mid-ventricle in the RVFW of healthy rats. The average peak E_{cc} was found to be -0.20 ± 0.01 at the base and -0.21 ± 0.02 at the mid-ventricle, which is in good agreement with previous studies using DENSE MRI (Suever et al., 2017), as well as strain-encoding MRI (Hamdan et al., 2008; Youssef et al., 2008), which all report values in the range of -0.18 to -0.20. Additionally, the average peak E_{ll} value of -0.16 ± 0.02 at the base is in agreement with the value of -0.16 reported by Fine et al. (2013b), and the mid-ventricle value of -0.18 ± 0.02 is consistent with the previously reported value of -0.18 (Hamdan et al., 2008; Suever et al., 2017).

The average peak E_{cc} was found to be significantly higher than peak E_{ll} at the mid-ventricular free wall (-0.21 ± 0.02 vs. -0.18 ± 0.02, $p < 0.002$). To further explore this, the present study also quantified strains in different segments of the RV. First, no regional differences were found for the peak E_{cc} at the base or mid-ventricle, which is consistent with Vigneault et al. (2016). However, regional differences in E_{ll} were solely detected in the anterior segment of both the base and mid-ventricle of the RVFW. More specifically, the strain was significantly lower in the anterior portion of the wall when compared to the other segments.

To elucidate this finding, the difference in longitudinal strain in the anterior segment could be influenced by the interaction of the RV and LV in that region (Rüssel et al., 2009; Zhang et al., 2017; Zhong et al., 2011). This is potentially due to the counterclockwise direction of twisting relative to the RV insertion point, as well as myofiber orientation (Doste et al., 2019), which alters motion in the anterior region. Interestingly, previous studies on healthy rats revealed that torsion and longitudinal strain in the LV were significantly lower on the anterior side when compared to other segments, while the circumferential strain showed no regional differences (Zhang et al., 2017). Combined with the results in the RV, this implies there is a bi-ventricular difference in the anterior longitudinal deformation.

4.1. Limitations

Since only the normal rat RV was investigated, one limitation is that no observations were conducted in animals with known cardiomyopathy or under treatment. Future work will include the assessment of RV dysfunction in a rat model. The apical slices could not be resolved due to the partial voluming of blood and myocardium, which caused a blurring effect in the images. Overall, the image quality of the apical slice was inadequate for resolving the RV strains. As imaging technologies and spatial resolution continue to advance, it may be possible to assess transmurally varying principal strains, in order to gain insights on cardiomyocyte deformation in the RV.

5. Conclusion

A preliminary study was performed on regional RV strains in the healthy rat heart using DENSE MRI. A new custom plugin

was developed in order to more accurately capture the sharp curvature of the rat RV. The custom plugin can potentially extend the applicability of the framework, for analyzing DENSE images, to other complicated topologies. Average basal and mid-ventricular strains agree with the findings of previous studies. Peak longitudinal strain exhibited regional differences at the base and mid-ventricle, as well as the anterior segment. This could be related to the relative deformation near the insertion point.

Declaration of Competing Interest

None of the authors have any commercial or other interest that are in conflict with the integrity of this work.

Acknowledgements

This study was supported by a grant from the National Science Foundation (CMMI-1538754), as well as grants from the National Institutes of Health (U01HL133359 and S10RR029541).

References

Benjamin Emelia, J., Muntner, P., Alonso, A., Bittencourt Marcio, S., Callaway Clifton, W., Carson April, P., Chamberlain Alanna, M., Chang Alexander, R., Cheng, S., Das Sandeep, R., Delling Francesca, N., Djousse, L., Elkind Mitchell, S.V., Ferguson Jane, F., Fornage, M., Jordan Lori, C., Khan Sadiya, S., Kissela Brett, M., Knutson Kristen, L., Kwan Tak, W., Lackland Daniel, T., Lewis Tené, T., Lichtman Judith, H., Longenecker Chris, T., Loop Matthew, S., Lutsey Pamela, L., Martin Seth, S., Matsushita, K., Moran Andrew, E., Mussolino Michael, E., O'Flaherty, M., Pandey, A., Perak Amanda, M., Rosamond Wayne, D., Roth Gregory, A., Sampson Uchechukwu, K.A., Satou Gary, M., Schroeder Emily, B., Shah Svati, H., Spartano Nicole, L., Stokes, A., Tirschwell David, L., Tsao Connie, W., Turakhia Mintu, P., VanWagner Lisa, B., Wilkins John, T., Wong Sally, S., Virani Salim, S., 2019. Heart disease and stroke statistics—2019 update: a report from the American Heart Association. Circulation 139, e56–e66.

Derrick, G.P., Josen, M., Vogel, M., Henein, M.Y., Shinebourne, E.A., Redington, A.N., 2001. Abnormalities of right ventricular long axis function after atrial repair of transposition of the great arteries. Heart 86, 203–206.

Doste, R., Soto-Iglesias, D., Bernardino, G., Alcaine, A., Sebastian, R., Giffard-Roisin, S., Sermesant, M., Berruezo, A., Sánchez-Quintana, D., Camara, O., 2019. A rule based method to model myocardial fiber orientation in cardiac biventricular geometries with outflow tracts. Int. J. Num. Meth. Biomed. Eng. 35, e3185.

Eyskens, B., Weidemann, F., Kowalski, M., Bogaert, J., Dymarkowski, S., Bijnens, B., Gewillig, M., Sutherland, G., Mertens, L., 2004. Regional right and left ventricular function after the Senning operation: an ultrasonic study of strain rate and strain. Cardiol. Young 14, 255–264.

Fine, N.M., Chen, L., Bastiansen, P.M., Frantz, R.P., Pellikka, P.A., Oh, J.K., Kane, G.C., 2013a. Outcome prediction by quantitative right ventricular function assessment in 575 subjects evaluated for pulmonary hypertension. Circul. Cardiovas. Imag. 6, 711–721.

Fine, N.M., Shah, A.A., Han, I.-Y., Yu, Y., Hsiao, J.-F., Koshino, Y., Saleh, H.K., Miller, F. A., Oh, J.K., Pellikka, P.A., Villarraga, H.R., 2013b. Left and right ventricular strain and strain rate measurement in normal adults using velocity vector imaging: an assessment of reference values and intersystem agreement. Int. J. Cardiovasc. Imag. 29, 571–580.

Gilliam, A.D., Suever, J.D., et al., 2016. DENSEanalysis. Retrieved from https://github.com/denseanalysis/denseanalysis.

Haber, I., Metaxas, D.N., Axel, L., 2000. Three-dimensional motion reconstruction and analysis of the right ventricle using tagged MRI. Med. Image Anal. 4, 335–355.

Haggerty, C.M., Kramer, S.P., Binkley, C.M., Powell, D.K., Mattingly, A.C., Charnigo, R., Epstein, F.H., Fornwalt, B.K., 2013. Reproducibility of cine displacement encoding with stimulated echoes (DENSE) cardiovascular magnetic resonance for measuring left ventricular strains, torsion, and synchrony in mice. J. Cardiovasc. Magn. Reson. 15, 71.

Hamdan, A., Thouet, T., Sebastian, K., Paetsch, I., Gebker, R., Wellnhofer, E., Schnackenburg, B., Fahmy, A.S., Osman, N.F., Fleck, E., 2008. Regional right ventricular function and timing of contraction in healthy volunteers evaluated by strain-encoded MRI. J. Magn. Reson. Imag. Off. J. Int. Soc. Magn. Reson. Med. 28, 1379–1385.

Labinskyy, N., Csiszar, A., Wu, J.M., Ballabh, P., Mathew, R., Podlutsky, A., Wolin, M. S., Ungvari, Z., 2008. Resveratrol prevents monocrotaline-induced pulmonary hypertension in rats. Hypertension 22, 1203–1209.

Liu, Z.-Q., 2018. DENSE3D_Plugin_4CrescentOrgan. Retrieved from https://github.com/Zhan-Qiu-Liu/DENSE3D_Plugin_4CrescentOrgan.

Lollert, A., Emrich, T., Eichstädt, J., Kampmann, C., Abu-Tair, T., Turial, S., Düber, C., Kreitner, K.-F., Staatz, G., 2018. Differences in myocardial strain between pectus excavatum patients and healthy subjects assessed by cardiac MRI: a pilot study. Eur. Radiol. 28, 1276–1284.

Meador, W.D., Malinowski, M., Jazwiec, T., Goehler, M., Quay, N., Timek, T.A., Rausch, M.K., 2018. A fiduciary marker-based framework to assess heterogeneity and anisotropy of right ventricular epicardial strains in the beating ovine heart. J. Biomech. 80, 179–185.

Morris, D.A., Krisper, M., Nakatani, S., Köhncke, C., Otsuji, Y., Belyavskiy, E., Radha Krishnan, A.K., Kropf, M., Osmanoglou, E., Boldt, L.-H., Blaschke, F., Edelmann, F., Haverkamp, W., Tschöpe, C., Pieske-Kraigher, E., Pieske, B., Takeuchi, M., 2017. Normal range and usefulness of right ventricular systolic strain to detect subtle right ventricular systolic abnormalities in patients with heart failure: a multicentre study. Eur. Heart J. Cardiovas. Imag. 18, 212–223.

Mouchaers, K.T.B., Schalij, I., Boer, M.A.D., Postmus, P.E., Hinsbergh, V.W.M.v., Amerongen, G.P.v.N., Noordegraaf, A.V., Laarse, W.J.v.d., 2010. Fasudil reduces monocrotaline-induced pulmonary arterial hypertension: comparison with bosentan and sildenafil. Eur. Respirat. J. 36 (4), 800–807.

Nucifora, G., Prati, G., Vitrella, G., Allocca, G., Cukon Buttignoni, S., Muser, D., Morocutti, G., Pinamonti, B., Sinagra, G., Selvanayagam, J., Proclemer, A., 2016. Right ventricular strain and dyssynchrony assessment in arrhythmogenic right ventricular cardiomyopathy: a cardiac magnetic resonance feature-tracking study. Heart Lung Circul. 25, S248.

Polak, J.F., Holman, B.L., Wynne, J., Colucci, W.S., 1983. Right ventricular ejection fraction: an indicator of increased mortality in patients with congestive heart failure associated with coronary artery disease. J. Am. Coll. Cardiol. 2, 217–224.

Rüssel, I.K., Tecelão, S.R., Kuijer, J.P., Heethaar, R.M., Marcus, J.T., 2009. Comparison of 2D and 3D calculation of left ventricular torsion as circumferential-longitudinal shear angle using cardiovascular magnetic resonance tagging. J. Cardiovasc. Magn. Reson. 11, 8.

Ryan, J.J., Huston, J., Kutty, S., Hatton, N.D., Bowman, L., Tian, L., Herr, J.E., Johri, A.M., Archer, S.L., 2015. Right ventricular adaptation and failure in pulmonary arterial hypertension. Can. J. Cardiol. 31, 391–406.

Sachdev, A., Villarraga, H.R., Frantz, R.P., McGoon, M.D., Hsiao, J.-F., Maalouf, J.F., Ammash, N.M., McCully, R.B., Miller, F.A., Pellikka, P.A., Oh, J.K., Kane, G.C., 2011. Right ventricular strain for prediction of survival in patients with pulmonary arterial hypertension. Chest 139, 1299–1309.

Sawamura, F., Kato, M., Fujita, K., Nakazawa, T., Beardsworth, A., 2009. Tadalafil, a long-acting inhibitor of PDE5, improves pulmonary hemodynamics and survival rate of monocrotaline-induced pulmonary artery hypertension in rats. J. Pharmacol. Sci. 111, 235–243.

Spottiswoode, B.S., Zhong, X., Hess, A.T., Kramer, C.M., Meintjes, E.M., Mayosi, B.M., Epstein, F.H., 2007. Tracking myocardial motion from cine DENSE images using spatiotemporal phase unwrapping and temporal fitting. IEEE Trans. Med. Imag. 26, 15–30.

Suever, J.D., 2016. dense3D_plugin. Retrieved from https://github.com/suever/dense3D_plugin/tree/biventricular.

Suever, J.D., Wehner, G.J., Jing, L., Powell, D.K., Hamlet, S.M., Grabau, J.D., Mojsejenko, D., Andres, K.N., Haggerty, C.M., Fornwalt, B.K., 2017. Right ventricular strain, torsion, and dyssynchrony in healthy subjects using 3D spiral cine DENSE magnetic resonance imaging. IEEE Trans. Med. Imag. 36, 1076–1085.

Vigneault, D.M., te Riele, A.S.J.M., James, C.A., Zimmerman, S.L., Selwaness, M., Murray, B., Tichnell, C., Tee, M., Noble, J.A., Calkins, H., Tandri, H., Bluemke, D.A., 2016. Right ventricular strain by MR quantitatively identifies regional dysfunction in patients with arrhythmogenic right ventricular cardiomyopathy. J. Magn. Reson. Imag. 43, 1132–1139.

Youssef, A., Ibrahim, E.-S.H., Korosoglou, G., Abraham, M.R., Weiss, R.G., Osman, N.F., 2008. Strain-encoding cardiovascular magnetic resonance for assessment of right-ventricular regional function. J. Cardiovasc. Magn. Reson. 10, 33.

Zhang, X., Liu, Z.-Q., Singh, D., Wehner, G.J., Powell, D.K., Campbell, K.S., Fornwalt, B. K., Wenk, J.F., 2017. Regional quantification of myocardial mechanics in rat using 3D cine DENSE cardiovascular magnetic resonance. NMR Biomed. 30, e3733.

Zhang, X., Liu, Z.-Q., Singh, D., Powell, D.K., Chung, C.S., Campbell, K.S., Wenk, J.F., 2019. Differential effects of isoproterenol on regional myocardial mechanics in rat using 3D cine DENSE cardiovascular magnetic resonance. J. Biomech. Eng. 141, 060904.

Zhong, X., Gibberman, L.B., Spottiswoode, B.S., Gilliam, A.D., Meyer, C.H., French, B. A., Epstein, F.H., 2011. Comprehensive Cardiovascular magnetic resonance of myocardial mechanics in mice using three-dimensional cine DENSE. J. Cardiovasc. Magn. Reson. 13, 83.